Evaluations and enhancements of fatigue crack initiation criteria for steels subjected to large shear deformations

International Journal of Fatigue 182 (2024) 108227

Contents lists available at ScienceDirect

International Journal of Fatigue

journal homepage: www.elsevier.com/locate/ijfatigue

Evaluations and enhancements of fatigue crack initiation criteria for steels subjected to large shear deformations

Nasrin Talebi [a,*], Johan Ahlström [b], Magnus Ekh [a], Knut Andreas Meyer [c]

[a] Division of Material and Computational Mechanics, Department of Industrial and Materials Science, Chalmers University of Technology, SE-412 96 Gothenburg, Sweden

[b] Division of Engineering Materials, Department of Industrial and Materials Science, Chalmers University of Technology, SE-412 96 Gothenburg, Sweden

[c] Institute of Applied Mechanics, TU Braunschweig, DE-38106 Braunschweig, Germany

ARTICLE INFO

Keywords:
Anisotropy
Crack initiation criteria
Tension–torsion tests
Large deformations
Finite element simulations

ABSTRACT

While large accumulated plastic deformations occur in the rail surface layer where rolling contact fatigue cracks initiate, many available Low Cycle Fatigue (LCF) crack initiation criteria focus on small plastic strains. Accordingly, this paper evaluates available fatigue crack initiation criteria for highly shear-deformed R260 steels, reflecting the conditions in the surface layer of rails. Furthermore, modified crack initiation criteria are suggested. The evaluation is based on three different experiments: Large shear strain increments under varying axial loading (predeformation), strain-controlled LCF tests after some predeformation, and axial High Cycle Fatigue (HCF) experiments. For the predeformation, Finite Element (FE) simulations, with a large-strain plasticity model for cyclic and distortional hardening, provide predictions of the local stress and strain histories. A cross-validation procedure is used to assess the accuracy and reliability of both established and modified fatigue crack initiation criteria. The proposed modifications to one of the criteria show an improved fit to the experimental data. However, there is a tendency to overfitting, which can be improved by including more experimental data.

1. Introduction

Rolling Contact Fatigue (RCF) in rails and wheels is recognized as a major source of problems in the railway industry [1], causing high maintenance costs [2]. For instance, the cost of RCF in rails was estimated at 150 MEUR per year by Deutsche Bahn [3]. Enhancing the accuracy of fatigue damage prediction models is a great challenge in railway engineering, which can contribute to increasing maintenance planning reliability and traffic safety.

RCF crack initiation is often connected to accumulated plastic deformations in the surface layer of rails and wheels. These plastic deformations align the cementite lamellae within the grains in pearlitic steel, resulting in anisotropic behavior [4]. To investigate the properties of this anisotropic surface layer, several experimental techniques have been developed and used. Wetscher et al. [5] used an equal channel angular pressing method to severely deform R260 pearlitic steel and found that the ultimate tensile stress, fracture toughness, and crack propagation rate of the material were influenced by the alignment of the microstructure. Leitner et al. [6], performed high-pressure-torsion tests on fully pearlitic steel and showed that fatigue crack resistance along the aligned cementite lamellae was reduced noticeably such that the fatigue cracks preferably propagated along the elongated microstructure. Meyer et al. [7] developed an experimental method to heavily deform pearlitic R260 rail steel in an axial-torsion machine. It was shown that the steel in the test bars reflected the properties and microstructure of the material in the field samples. An advantage of this technique is that the deformed test bars can be used for further multiaxial testing to investigate the cyclic behavior of the material. In the present study, to evaluate different crack initiation criteria, the experimental results from this method are used as one part of calibration data.

Many crack initiation criteria for rolling contact conditions have been proposed in literature, see, e.g. the reviews by Sadeghi et al. [8] and Ringsberg et al. [9]. Kapoor [10] suggested that ratcheting damage evolution is associated with ratcheting strain in each loading cycle, and crack initiation occurs when ratcheting strain reaches a critical value. While this criterion is computationally efficient, it does not account for the mean stress effect, which is found to be influential on fatigue performance [7]. A strain energy density fatigue criterion was developed by Golos and Ellyin [11]. Fatigue damage increment in each loading cycle is based on total strain energy density additively decomposed

* Corresponding author.
E-mail address: nasrin.talebi@chalmers.se (N. Talebi).

https://doi.org/10.1016/j.ijfatigue.2024.108227
Received 13 November 2023; Received in revised form 8 February 2024; Accepted 19 February 2024
Available online 21 February 2024

into plastic and tensile elastic strain energy density facilitating crack growth.

In contrast to the Kapoor and Golos–Ellyin models, some criteria are based on a critical plane search approach seeking the plane with the largest amount of fatigue damage, where macrocracks are assumed to initiate. One early such model was proposed by Brown and Miller [12], considering the fatigue life to be based on the maximum shear strain and tensile strain occurring on the plane of maximum shear strain. An energy-density based multiaxial LCF criterion for non-proportional loading was formulated by Jiang and Sehitoglu [13], where normal and shear stress and strain ranges contribute to damage evolution on a given plane. Moreover, they modified the criterion to consider ratcheting damage in each loading cycle as well. Ince and Glinka [14] proposed an extended multiaxial damage parameter (Generalized Strain Energy) compared to the J-S criterion, which has elastic and plastic strain energy density terms obtained from normal and shear stress and strain ranges on a crack plane.

There are also criteria, such as the one proposed by Franklin et al. [15], that consider the microstructure in the fatigue damage predictions, which is important in rolling contact fatigue. Trummer et al. [16] proposed a crack initiation criterion by considering the effect of large plastic deformations in an anisotropic layer close to the surface of wheels and rails, which is calibrated based on wheel-rail test rig experiments. A two-dimensional FE framework to investigate RCF at the microstructural level was developed by Ghodrati et al. [17]. Chaboche plasticity model was used for grain material, and material degradation of cohesive elements at the grain boundaries was defined based on the Jiang and Sehitoglu damage evolution law.

However, no criterion has been evaluated to consider the effect of large (pre)deformations, cyclic LCF experiments, and HCF endurance limit. As a starting point in this study, among the mentioned criteria, two commonly used crack initiation criteria in railway mechanics, i.e. the Jiang–Sehitoglu criterion considering LCF damage and the so-called mixed model accounting for both ratcheting and fatigue damage in each loading cycle, are chosen for further investigations.

The first objective of this paper is to investigate whether the established crack initiation criteria are applicable during large shear deformations inducing anisotropy in the surface layer of rails. To study this, data from three groups of experiments are considered: Pure predeformation tests with axial and torsional loading [7], predeformation with subsequent uniaxial or multiaxial proportional cyclic loading [18], and HCF tests to identify the fatigue damage threshold [19]. In order to estimate the local stress and strain histories as accurately as possible (which will be used in the fatigue life predictions), FE simulations of the predeformation tests are done in Abaqus using the finite strain plasticity model developed by Meyer and Menzel [20] accounting for cyclic and distortional (anisotropic) hardening. A cross-validation approach is adopted to evaluate the capabilities of the crack initiation criteria. The results in terms of the identified fatigue parameters as well as the fitting and prediction errors are discussed. As the criteria results showed room for improvement, the paper's second objective is to enhance the Jiang and Sehitoglu criterion, with the aim of improving its fitting and predictive abilities. The paper presents and discusses the results of such modified criteria.

2. Experiments

As mentioned in the introduction, results from three different types of previously conducted experiments have been used to evaluate the crack initiation criteria: Pure predeformation tests, multiaxial cyclic LCF tests combined with predeformation, and HCF experiments. The non-standard experimental procedures for the former two are briefly described in Sections 2.1 and 2.2, respectively.

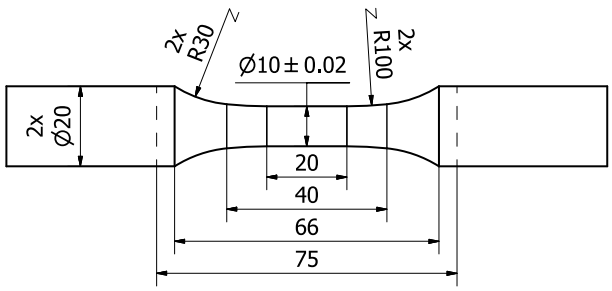

Fig. 1. Test bar dimensions in mm in pure predeformation tests [7].

Table 1
Considered predeformation tests. σ_a and N_f denote the nominal stresses and the number of cycles to failure, respectively.

Test name	σ_a [MPa]	N_f
PD(−500)	−500	8.16
PD(−250)	−250	5.17
PD(0)	0	3.22
PD(+250)	+250	2.44

2.1. Pure predeformation tests

An experimental method to replicate the large shear strains and anisotropy in the surface layers of in-service rails has been developed by Meyer et al. [7]. The experimental procedure described in this section has been explained in detail in [7]. Solid cylindrical test bars, with dimensions according to Fig. 1, were extracted from virgin pearlitic R260 railheads along the rolling direction. The following experimental procedure applied to these test bars constitutes one part of the calibration data in the present study.

The bars were subjected to twist in steps of 90° under constant axial loading according to the procedure described in Fig. 2(a). The purpose is to obtain similar loading conditions to those in the surface layer of rails. Four different nominal axial stresses were applied: −500, −250, 0, and +250 MPa, where the maximum compressive stress was limited to −500 MPa to avoid buckling. Fig. 2(b) (top) shows the undeformed test bar, and large shear strains visualized by laser-etched grids are illustrated in Fig. 2(b) (bottom). All test bars were predeformed until the torque dropped 2 N m below the maximum value in the current loading cycle, and visible cracks on the specimens were observed at this point. The number of cycles to failure for each test is presented in Table 1. As can be seen, the fatigue lives are very short, since large biaxial strains occur in each predeformation cycle.

Meyer et al. [18] found that predeformation does not significantly affect elastic parameters (e.g. less than 4% and 1% change in the shear modulus and Young's modulus respectively, after 6 cycles of predeformation). This observation motivates the use of a plasticity model without continuum damage (that would cause a degradation of the elastic stiffness). The results in terms of the torque responses for the four axial stresses are shown in Fig. 7(a). As can be seen, axial loading has a significant influence on the failure twist angle. The combined shear and tension–compression loading condition in this method is similar to that in rolling contacts (see e.g. [21,22]). It should be noted there is an overlap between the axial and torsional loading, which is an important parameter when studying rolling contact fatigue as discussed in Wong et al. [23]. In the pure predeformation tests, high levels of shear strains can be achieved. As an example, it was 2.3 after 8 cycles of predeformation in a specimen under the nominal compressive stress of −500 MPa [7]. Furthermore, the crack initiation takes place in anisotropic material. These facts make the test results suitable for studying fatigue properties and behavior of the rail surface layer.

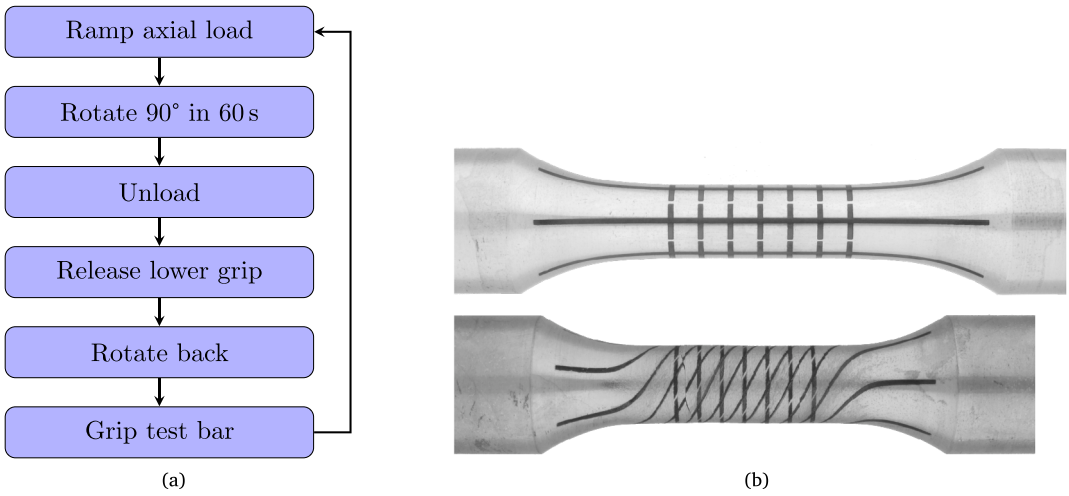

Fig. 2. (a) The predeformation procedure, and (b) Undeformed (top) and deformed (bottom) test bars [7].

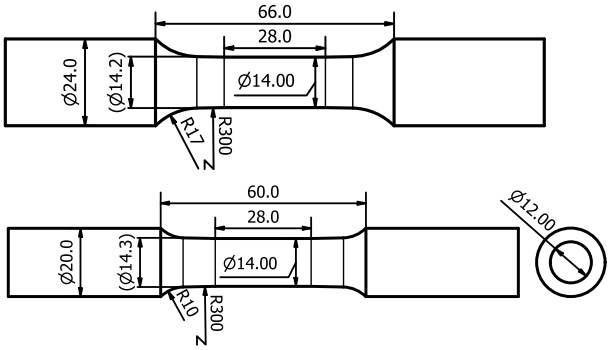

Fig. 3. The dimensions of solid (top) and thin-walled (bottom) test bars in mm in the cyclic tests [18].

2.2. Uniaxial and proportional multiaxial alternating cyclic tests

A limitation of the pure predeformation tests is that there are very few loading cycles until failure. Therefore, low cycle fatigue tests, for both virgin and predeformed material, are considered as well. Meyer et al. [18] slightly modified the predeformation experiments from [7] to facilitate the manufacturing of thin-walled tubular test bars. They used an updated specimen geometry (see the upper drawing in Fig. 3) and changed the nominal compressive stress from −500 MPa to −600 MPa. In addition to the undeformed cases, two levels of predeformation (3 and 6 steps) were investigated. Since there is a shear strain gradient over the cross-section of the solid test bars, the deformation field is inhomogeneous. To increase the homogeneity, the predeformed bars were remachined into a thin-walled tubular shape with an inner diameter of 12 mm and an outer diameter of 14 mm [18], see the lower drawing in Fig. 3.

After remachining, the predeformed tubular test bars were subjected to cyclic loading in different directions in $\epsilon_{zz}-\epsilon_{z\theta}$ plane. It was assumed that the only non-zero stress components are σ_{zz} and $\sigma_{z\theta}$. The mean stresses over the wall thickness $\bar{\sigma}_{zz}$ and $\bar{\sigma}_{z\theta}$ are calculated as in [18]

$$\bar{\sigma}_{zz} = \frac{F_a}{\pi\left(r_o^2 - r_i^2\right)} \tag{1}$$

$$\bar{\sigma}_{z\theta} = \frac{2T}{\pi\left(r_o^2 - r_i^2\right)\left(r_o + r_i\right)} \tag{2}$$

where F_a and T are the applied axial force and torque, respectively, and r_i and r_o are inner and outer radii. The axial strain $\epsilon = \epsilon_{zz}$ and the rotation φ over the gauge length L_g=12 mm were measured by the extensometer [18]. The mean shear strain is calculated (and will be used in the damage predictions) as

$$\gamma = 2\bar{\epsilon}_{z\theta} = \frac{\varphi\left(r_o + r_i\right)}{2L_g} \tag{3}$$

Plastic incompressibility is assumed, whereby the following relation between the normal strains is adopted: $\epsilon_{rr} = \epsilon_{\theta\theta} = -0.5\epsilon_{zz}$. The shear strains ϵ_{rz} and $\epsilon_{r\theta}$ are assumed to be zero.

The specimens were subjected to symmetric cyclic loading, with a 0.8% von Mises strain amplitude, until complete failure happened. Note that the fatigue crack propagation regime was found to be negligible (i.e., less than 1.1% of the total life). Table 2 lists the cyclic tests considered in this paper with crack initiation inside the gauge section. The evolution of stress ranges in the cyclic tests with pure axial and torsional loading is shown in Fig. 4. It can be seen that an increase in the predeformation level results in larger stress ranges caused by the fact that a larger amount of predeformation gives a more work-hardened material [18]. In the following strain-controlled fatigue tests, the higher stress amplitudes yield shorter fatigue lives.

Table 2
Considered cyclic tests. PD_x and N_f denote x cycles of predeformation and the number of cycles to failure, respectively.

Test name	Loading mode	N_f	ϵ_a [%]	γ_a [%]
PD_0-Shear	Pure torsion	2237	–	1.3
PD_3-Shear	Pure torsion	1368	–	1.3
PD_3-Axial	Pure axial	632	0.8	–
PD_3-Mixed	Mixed	1331	0.3	1.2
PD_6-Axial	Pure axial	292	0.8	–

3. Modeling of predeformation tests

To evaluate different crack initiation criteria, stress and strain histories are required. In the pure predeformation tests and the predeformation part of the cyclic tests, only the specimen's elongation, axial force, twist, and torque have been measured [7] (since the condition was inhomogeneous). Therefore, FE analyses are done to extract local stress and strain histories during predeformation.

3.1. Finite element model

The FE simulations are conducted in the commercial FE code Abaqus [24] using 8-node quadratic axisymmetric elements with reduced integration and additional degrees of freedom for twist (referred

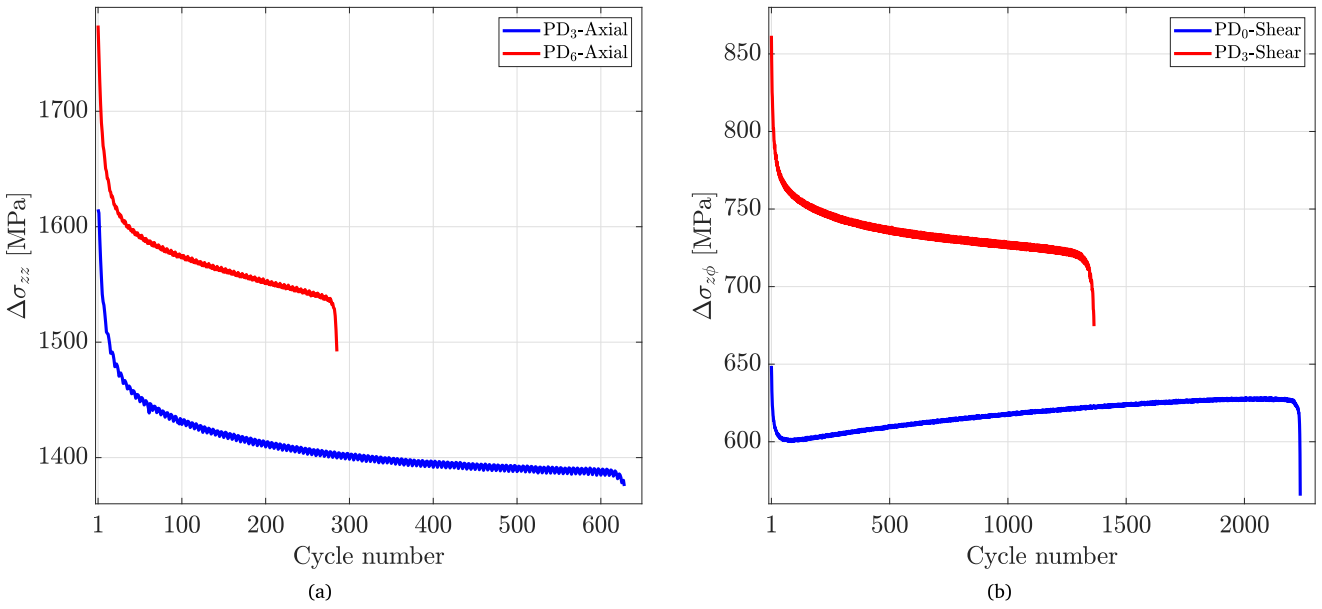

Fig. 4. Stress ranges for the strain-controlled cyclic tests: (a) Pure axial loading tests, and (b) pure shear loading tests.

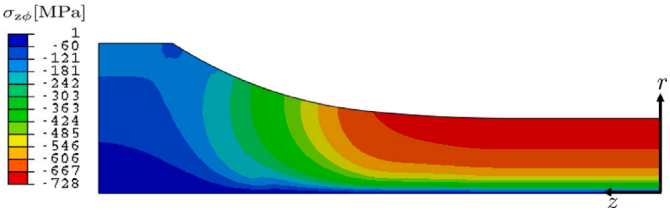

Fig. 5. Shear stresses for the test bar with 10 mm gauge diameter at the end of the 8th predeformation cycle, before unloading, at $\sigma_a = -500$ MPa.

to as CGAX8R in Abaqus element code). This means that while the element discretization is done in the 2D axisymmetric plane, the degrees of freedom in the nodes are displacements in the radial $u_r(r, z)$ and z-direction $u_z(r, z)$ as well as twist $\varphi(r, z)$. In the FE model of the pure predeformation tests, a 0.8 mm mesh size is chosen to give accurate enough results for the stresses and strains. The shear stresses at the end of the 8th predeformation cycle, before unloading, at $\sigma_a = -500$ MPa are shown in Fig. 5, where $\sigma_{z\phi}$ increases from the center to the surface of the specimen. For the predeformation part of the cyclic tests, the analyzed local stress and strain histories are extracted from the point where the experimental data during the cyclic tests on the tubular test bars were recorded. Specifically, with the mesh size 0.3 mm, the results have been extracted at $r = 6.57$ mm and $z = 0.07$ mm in the PD_3 tests and at $r = 6.52$ mm and $z = 0.06$ mm in the PD_6 test, respectively.

3.2. Material model

The reliability of the extracted stress and strain histories from the FE simulations is dependent on the accuracy of the material model. Therefore, a material model formulation must account for the mechanisms in the material such as yielding, cyclic hardening (for proportional and non-proportional loading), and anisotropy evolution. In this paper, we adopt a finite strain model formulation proposed by Meyer and Menzel [20], where parameter identification has been done for the R260 rail steel.

The model is based on the compressible isotropic Neo-Hookean hyperelastic free energy. The evolving anisotropic yield criterion is formulated as

$$\Phi = \sqrt{\boldsymbol{M}^{\text{dev}}_{\text{red}} : \hat{\mathbf{C}} : \boldsymbol{M}^{\text{dev}}_{\text{red}}} - Y \leq 0 \tag{4}$$

where $\hat{\mathbf{C}}$ is the evolving anisotropy tensor, $\boldsymbol{M}^{\text{dev}}_{\text{red}}$ is the reduced deviatoric Mandel stress, and Y is the isotropic hardening. In this paper, we introduced an additional back-stress compared to the number of back-stresses in [20], resulting in $N_{\text{back}} = 3$, to avoid unphysical strain localization in the FE simulations of PD(0) and PD(+250) tests. The evolution of the yield surface at $\sigma_a = -500$ MPa is shown in Fig. 6. While the initial yield surface (red) is isotropic, the ratio of the vertical axis ($\sqrt{3}\sigma_{z\phi}$) to the horizontal axis (σ_{zz}) of the yield surface after 8 cycles of predeformation (blue) is 1.11, i.e. an anisotropic yield surface. Fig. 6 also shows a shrinkage of the yield surface (softening). This behavior is supported by the experimental observations of a similar material in [25], where the yield surface shrinks with increased plasticity. The open-source implementation [26] of the material model as a user subroutine (UMAT) for Abaqus has been used. It uses the implicit backward Euler time discretization scheme. A more detailed description of the material model and its parameters are given in Appendix.

3.3. Modeling results

The simulated torque versus twist for the pure predeformation tests with four different nominal axial stresses are shown in Fig. 7(b). It can be noted that the maximum torque in each loading cycle is overpredicted. Compared to the experiments, in the PD(0) test, the torque is noticeably highest in the first two cycles and then saturates. Furthermore, the elastic to plastic transition is smoother in the simulations than that in the experiments. It is considered that the material model predicts the experimental results rather well, and the FE results are accurate enough for evaluating fatigue criteria.

The time histories of the true stresses and logarithmic strains are illustrated in Fig. 8. The evaluation point is close to the surface and in the middle of the gauge length of the specimens. In all cases, the true stress σ_{zz} has approximately reached the applied nominal stress after the first application of the axial load. The magnitude of the true axial stress decreases during torsional loading, which is caused by an increase in the gauge diameter. Upon unloading, residual axial and shear stresses develop due to stress gradients. The tensile axial residual stresses can affect the fatigue damage predictions, see Section 4.

The reduction in the gauge diameter due to the tensile loading causes the localization of shear strains in the gauge section (note that large deformations happen during the predeformation). The increment in the ratcheting shear strain is larger for the tensile loading compared

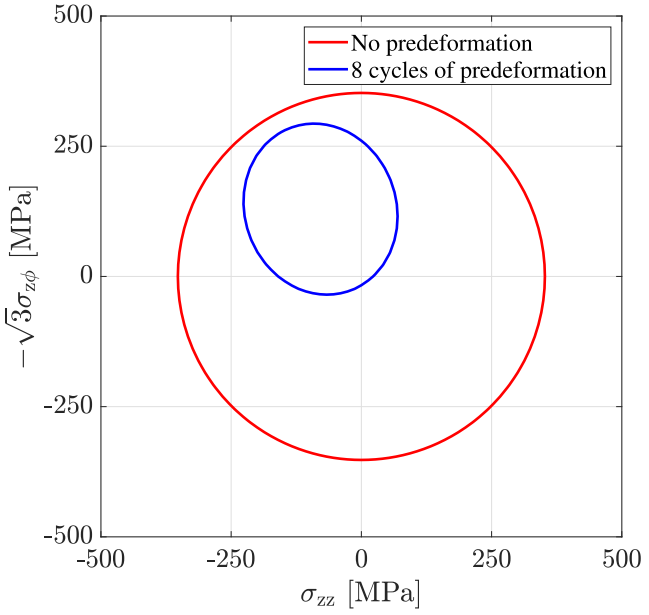

Fig. 6. Yield surface evolution described by the material model in [20] without predeformation (red) and at the end of the 8th (blue) predeformation cycle at $\sigma_a = -500$ MPa for a test bar with 10 mm gauge diameter. The evaluation point is at $z = 0.18$ mm and $r = 4.89$ mm.

to that for the compressive loading. It should be noted that, even under tensile axial loading, ϵ_{zz} becomes negative due to the shear-induced rotations. This is caused by the definition of the logarithmic strain on the deformed configuration, see e.g. [24].

4. Crack initiation criteria

Three available crack initiation criteria from rolling contact fatigue literature are summarized in the following section and evaluated in Section 6. The assessment is based on the number of cycles to failure in the pure predeformation tests and the tests with predeformation followed by multiaxial cyclic loading (see Section 2).

4.1. Kapoor criterion

In the criterion proposed by Kapoor [10], it is assumed that LCF and ratcheting are two independent failure mechanisms, and the one that leads to earlier failure determines the life to macroscopic crack initiation. According to [10], the ratcheting damage increment per loading cycle can be formulated as

$$\frac{\mathrm{d}D_{\mathrm{r},i}}{\mathrm{d}N} = \frac{1}{\epsilon_{\mathrm{c}}}\frac{\mathrm{d}\epsilon_{\mathrm{vM}}}{\mathrm{d}N} \tag{5}$$

where ϵ_{c} is the critical ratcheting strain parameter, and $\mathrm{d}\epsilon_{\mathrm{vM}}/\mathrm{d}N$ is the von Mises strain increment per loading cycle defined as

$$\frac{\mathrm{d}\epsilon_{\mathrm{vM}}}{\mathrm{d}N} = \sqrt{\frac{2}{3}}\left(\left|\boldsymbol{\epsilon}^{\mathrm{dev}}(t_{\mathrm{end}})\right| - \left|\boldsymbol{\epsilon}^{\mathrm{dev}}(t_{\mathrm{start}})\right|\right) \tag{6}$$

$\boldsymbol{\epsilon}^{\mathrm{dev}}(t_{\mathrm{start}})$ and $\boldsymbol{\epsilon}^{\mathrm{dev}}(t_{\mathrm{end}})$ represent the deviatoric strain tensors at the beginning and at the end of each loading cycle, respectively. It is assumed that the ratcheting damage accumulates linearly, and when $D_{\mathrm{r}} = \sum_{i=1}^{N} \mathrm{d}D_{\mathrm{r},i}/\mathrm{d}N = 1$, macroscopic crack initiation happens. Although this criterion is computationally efficient, it does not consider the important influence of compressive or tensile stresses on the life span as was observed experimentally, see Section 2.

4.2. Jiang-Sehitoglu criterion

Jiang and Sehitoglu suggested a multiaxial low cycle fatigue criterion [13] (J-S criterion), which is based on the critical plane search approach. This is an important part of the model, especially in the case of non-proportional loading (as in the pure predeformation tests and the predeformation part of the cyclic tests), where the principal directions of the stress and strain tensors vary with time.

The fatigue driving force FP (denoted as "Fatigue Parameter" in [13]) on a given plane defined by the normal $\boldsymbol{n}$ is quantified as

$$FP = \frac{\Delta\epsilon}{2}\sigma_{\max} + J\,\Delta\gamma\,\Delta\tau \tag{7}$$

where $\Delta\epsilon$ is the normal strain range, $\sigma_{\max}$ is the maximum normal stress, $\Delta\gamma$ is the shear strain range, $\Delta\tau$ is the shear stress range, and J is a fatigue parameter. J defines the contribution of shear loading to FP and is calibrated against experimental data in Section 6. The mean stress effect is incorporated by using the maximum normal stress $\sigma_{\max}$ in each loading cycle, cf. [13]. Note that, for the brevity of presentation, hereafter, stress refers to true stress and strain refers to logarithmic strain (both tensors are defined in the current configuration). By searching all possible planes at a given material point, the critical plane is identified, where FP is maximum, i.e. $\max_{\boldsymbol{n}} FP$. The planes are defined by considering a unit sphere and varying the polar angle $\theta \in [0, \pi/2]$ and the azimuthal angle $\varphi \in [0, 2\pi]$. The Cartesian components of $\boldsymbol{n}$ are expressed as

$$\boldsymbol{n} = \begin{bmatrix} \sin(\theta)\cos(\varphi) \\ \sin(\theta)\sin(\varphi) \\ \cos(\theta) \end{bmatrix} \tag{8}$$

The stress vector $\boldsymbol{t}$ and the strain vector $\boldsymbol{t}_\epsilon$ on a given plane are obtained by using the normal vector $\boldsymbol{n}$

$$\boldsymbol{t} = \boldsymbol{\sigma}\cdot\boldsymbol{n}, \quad \boldsymbol{t}_\epsilon = \boldsymbol{\epsilon}\cdot\boldsymbol{n} \tag{9}$$

where $\boldsymbol{\sigma}$ and $\boldsymbol{\epsilon}$ are the stress and strain tensors, respectively. The projected normal stress σ and normal strain ϵ are computed as

$$\sigma = \boldsymbol{t}\cdot\boldsymbol{n}, \quad \epsilon = \boldsymbol{t}_\epsilon\cdot\boldsymbol{n} \tag{10}$$

whereas the projected shear stress $\boldsymbol{\tau}$ and shear strain $\boldsymbol{\gamma}$ are given by

$$\boldsymbol{\tau} = \boldsymbol{t} - \sigma\,\boldsymbol{n}, \quad \boldsymbol{\gamma} = 2\left(\boldsymbol{t}_\epsilon - \epsilon\,\boldsymbol{n}\right) \tag{11}$$

In addition, two time instances in a loading cycle must be identified that give the largest FP among all possible planes $\boldsymbol{n}$. Considering the two time instances t_1 and t_2, Δ_ϵ, Δ_τ, and Δ_γ are calculated as

$$\Delta\epsilon = \epsilon(t_1) - \epsilon(t_2) \tag{12}$$

and

$$\Delta\tau = \left|\boldsymbol{\tau}(t_1) - \boldsymbol{\tau}(t_2)\right|, \quad \Delta\gamma = \left|\boldsymbol{\gamma}(t_1) - \boldsymbol{\gamma}(t_2)\right| \tag{13}$$

The fatigue damage increment for loading cycle i is formulated as

$$\frac{\mathrm{d}D_{\mathrm{f},i}}{\mathrm{d}N} = \left(\frac{\langle \max_{\boldsymbol{n}} FP - FP_0\rangle}{C_0}\right)^m \tag{14}$$

where the symbol $\langle\bullet\rangle$ represents Macaulay bracket ($\langle\bullet\rangle = 1/2(\bullet + |\bullet|)$). m and C_0 are fatigue parameters, which are determined based on the considered experiments in Section 6. The fatigue parameter FP_0 has been identified from the HCF experiments on pearlitic rail steel Grade 900 A conducted by Christodoulou et al. [19]. Accordingly, in the J-S criterion, both LCF and HCF regions will be unified. The chemical composition of the rail steel Grade 900 A is similar to that of the pearlitic R260 rail steel used in Meyer et al. [27] (Table 1). The yield stresses $R_{\mathrm{p0.2}}$ of rail steel Grade 900 A in [19] and R260 in [27] are very close (533 MPa and 534.2 MPa, respectively). The stress-controlled axial HCF tests were conducted with a stress ratio of $R = 0.1$. From the obtained S-N curve, the fatigue limit, denoted as σ_{fl}, was evaluated as 540 MPa at a fatigue life of 10^7 [19]. By using the fatigue limit σ_{fl}

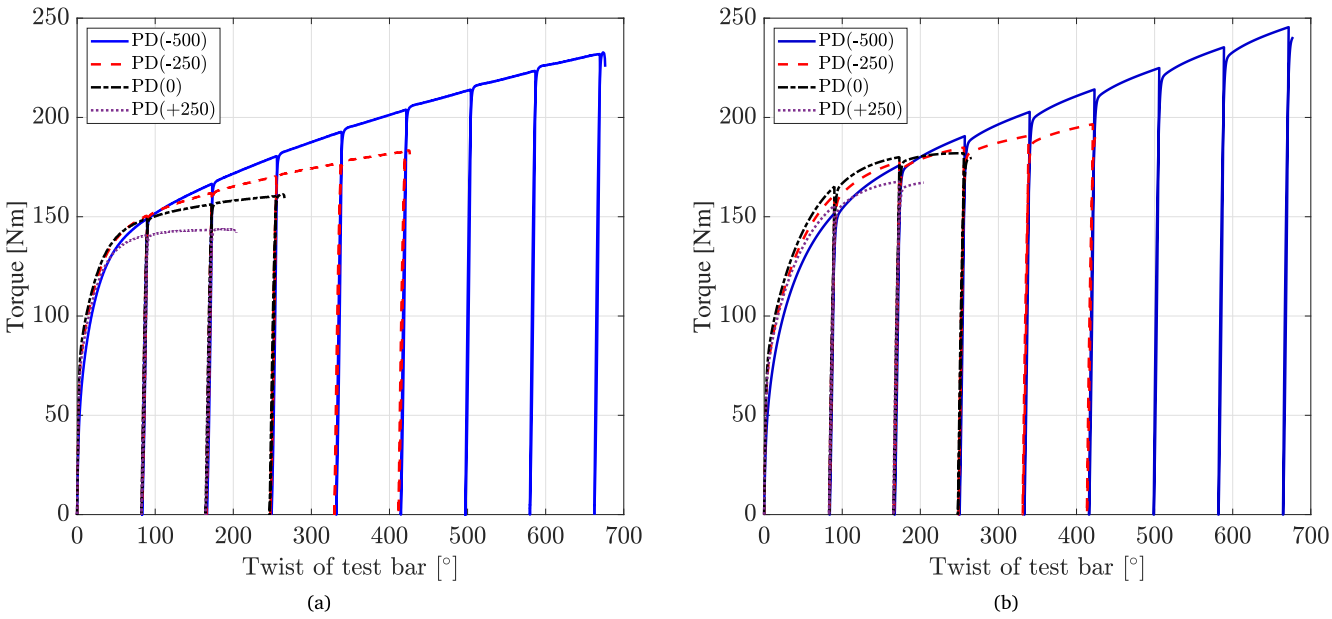

Fig. 7. Torque responses for the pure predeformation tests: (a) Experimental results, and (b) simulation results.

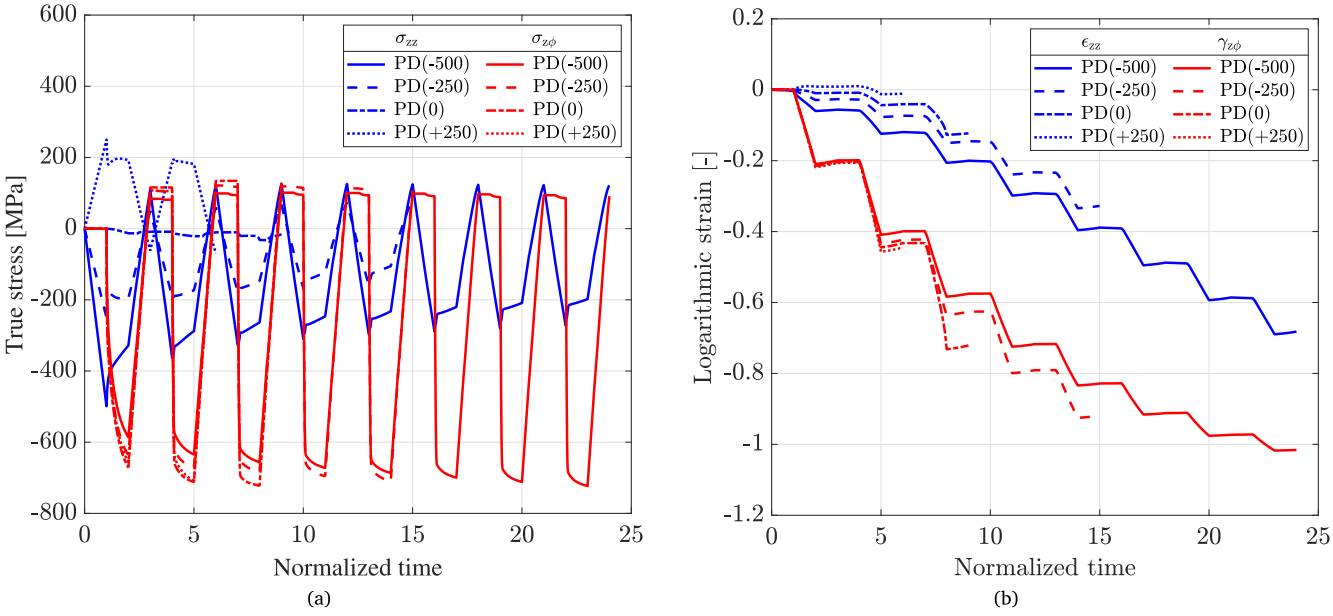

Fig. 8. Simulated stress and strain histories for the pure predeformation tests at $z = 0.18$ mm and $r = 4.89$ mm: (a) True stresses, and (b) logarithmic strains.

and the stress ratio R, the minimum normal stress $\sigma_{\min}$ and the normal stress range $\Delta\sigma$ are computed as

$$\sigma_{\min} = \sigma_{f1} R = 54 \text{ MPa} \tag{15a}$$

$$\Delta\sigma = \sigma_{f1} - \sigma_{\min} = 486 \text{ MPa} \tag{15b}$$

Since the material response is predominately elastic in HCF tests (on the macroscopic level), normal strain range $\Delta\epsilon$ is obtained as

$$\Delta\epsilon = \frac{\Delta\sigma}{E} = 0.002 \tag{16}$$

where E is Young's modulus of R260 rail steel from Table A.6. Then, by considering the normal loading term of Eq. (7), FP_0 is identified as

$$FP_0 = \frac{\Delta\epsilon}{2}\sigma_{f1} = 0.62 \text{ MPa} \tag{17}$$

Note that we have introduced the parameter C_0, which has the same dimension as FP instead of using C ($C = C_0^m$) as presented in [13] to avoid the dependence of the dimension of C on the exponent m. In the J-S criterion, the fatigue damage is assumed to accumulate linearly, and when the total damage equals unity, a macroscopic fatigue crack initiates.

4.3. Mixed criterion

Another criterion was suggested by Jiang and Sehitoglu [13], which linearly adds ratcheting and fatigue damage in each loading cycle. In contrast to the Kapoor criterion, it assumes that fatigue damage and ratcheting damage complement each other; when the ratcheting damage rate remains constant due to the saturation of ratcheting strain, the dominant failure mechanism is fatigue [13]. Macroscopic crack

initiation occurs when the total damage equals unity

$$D = \sum_{i=1}^{N} \left(\frac{\mathrm{d}D_{\mathrm{f},i}}{\mathrm{d}N} + \frac{\mathrm{d}D_{\mathrm{r},i}}{\mathrm{d}N} \right) = 1 \tag{18}$$

4.4. Modified Jiang–Sehitoglu criterion ($\widetilde{C_0}$)

As will be shown in Section 6, the mixed criterion does not give noticeably improved results compared to the J-S criterion for the considered experiments in this study, since predeformation has a beneficial influence on the fatigue behavior of the specimens. Therefore, the J-S criterion is improved to obtain a better fit between the experiments and simulations. To account for the material state which is affected by the predeformation (i.e., anisotropy and work hardening), one suggestion is to allow the dependence of C_0 on ratcheting strain. This is inspired by the work done by Gren and Ahström [28], where it was experimentally shown that the fatigue crack propagation rate is decreased when the material has been predeformed. Accordingly, we introduce $\widetilde{C_0}$ as a linear function of ratcheting strain

$$\widetilde{C_0}\left(\epsilon_{\mathrm{r}}\right) = C_0 + S\epsilon_{\mathrm{r}} \tag{19}$$

where S is a fatigue parameter. By this choice of $\widetilde{C_0}$, Eq. (14) is reformulated as

$$\frac{\mathrm{d}D_{\mathrm{f},i}}{\mathrm{d}N} = \left(\frac{\langle \max_{\boldsymbol{n}} FP - FP_0 \rangle}{\widetilde{C_0}} \right)^m \tag{20}$$

As the mixed criterion, this modified model has four fatigue parameters to be identified: m, C_0, J, and S. Note that, henceforth, this modified version of the J-S criterion will be denoted by "modified J-S criterion ($\widetilde{C_0}$)".

4.5. Modified Jiang–Sehitoglu criterion ($\widetilde{FP_0}$)

An alternative modification of the J-S criterion, which also considers the increase in the fatigue crack resistance caused by predeformation, is letting the fatigue threshold depend on the ratcheting strain. $\widetilde{FP_0}$ is thus introduced as a function of ratcheting strain, which is formulated as

$$\widetilde{FP_0}\left(\epsilon_{\mathrm{r}}\right) = FP_\infty - \left(FP_\infty - FP_0\right) \exp\left(\frac{-\epsilon_{\mathrm{r}}}{\kappa}\right) \tag{21}$$

where FP_∞ is the saturation value for $\widetilde{FP_0}$, and κ controls how fast this is asymptotically approached. Note that the threshold for an undeformed material is still FP_0, whereas, during predeformation, the threshold will get closer to FP_∞. Accordingly, Eq. (14) is reformulated as

$$\frac{\mathrm{d}D_{\mathrm{f},i}}{\mathrm{d}N} = \left(\frac{\left\langle \max_{\boldsymbol{n}} FP - \widetilde{FP_0} \right\rangle}{C_0} \right)^m \tag{22}$$

This criterion has five fatigue parameters to be determined: m, C_0, J, FP_∞, and κ. Hereafter, "modified J-S criterion ($\widetilde{FP_0}$)" refers to this modified version of the J-S criterion.

An alternative modification of the J-S criterion would be to allow $\widetilde{FP_0}$ depending on each plane's alignment with the microstructure. The microstructure orientation could be obtained from the anisotropy tensor, $\hat{\mathbf{C}}$, in the plasticity model. However, a much larger experimental campaign would be required to validate such a complex model. As discussed in Section 6, the proposed criterion (Eq. (22)), using stress and strain predictions that account for the plastic anisotropy, gives reasonably good results.

Table 3
Permissible intervals for fatigue parameters.

Parameter, p	Interval	Unit
m	[1.0, 3.0]	–
C_0	[60.0, 200.0]	MPa
J	[0.0, 1.0]	–
ϵ_{c}	[1.5, 20.0]	–
S	[0.0, 200.0]	MPa
FP_∞	[0.62, 4.00]	MPa
κ	(0.0, 1.0]	–

5. Parameter identification

To identify the fatigue parameters for the criteria discussed in Section 4, an iterative optimization algorithm has been used, minimizing the difference between the experiments and simulations in terms of the number of cycles to macroscopic crack initiation. The objective function is chosen to be of a least-square type and is formulated as

$$E_{\mathrm{obj}} = \frac{1}{\sqrt{N_{\mathrm{p}}}} \sqrt{\sum_{i=1}^{N_{\mathrm{p}}} \left(\frac{N_{\mathrm{f},i} - N_{\mathrm{s},i}}{N_{\mathrm{f},i}} \right)^2} \tag{23}$$

where $N_{\mathrm{f},i}$ and $N_{\mathrm{s},i}$ are the number of cycles to macroscopic crack initiation in the experiments and simulations, respectively. The index i denotes each test, and N_{p} refers to the total number of evaluated experiments. Due to different magnitudes of fatigue lives in the experiments (see Section 2), contributions to the objective function are normalized with the corresponding experimental results $N_{\mathrm{f},i}$. As can be noted in Table 1, N_{f} for each pure predeformation test is not presented as an integer number. The reason is that N_{f} in the pure predeformation tests is very low due to large deformations occurring in each cycle. Therefore, $N_{\mathrm{f},i}$ in the pure predeformation tests is calculated as

$$N_{\mathrm{f},i} = N + \frac{\left(\phi_i(t_{\mathrm{end}}) - \phi_i(t_{\mathrm{start}})\right)_{\mathrm{Last\ cycle}}}{\pi/2} \tag{24}$$

where N is the number of cycles before the failure cycle, and $\phi_i(t_{\mathrm{start}})$ and $\phi_i(t_{\mathrm{end}})$ are twist angles at the beginning and at the end of the last loading cycle in a pure predeformation test i, respectively.

The optimization procedure is conducted in two steps by using the gradient-free, Nelder–Mead simplex algorithm [29,30]. The first step starts with 200 initial guesses generated using Latin Hypercube sampling in the parameter space described in Table 3. From these, the first step of optimization is performed. Then, 20 sets of parameter values with the lowest E_{obj} are chosen as starting guesses for the second step of the optimization. Finally, the parameter set with the lowest E_{obj} is selected. To improve the convergence of the optimizations, each fatigue parameter is scaled to be $\hat{p} \in [0, 1]$ by introducing

$$\hat{p} := \frac{p - p_{\min}}{p_{\max} - p_{\min}} \tag{25}$$

where $p_{\max}$ and $p_{\min}$ are lower and upper bounds of p, respectively. The objective function is penalized if attempts are outside the permissible intervals from Table 3.

As mentioned in Section 4, failure occurs when the accumulated damage reaches unity. Accordingly, if the total damage is larger than (or equal to) 1, $N_{\mathrm{s},i}$ is obtained by doing a linear interpolation between the cycle number of two subsequent loading cycles (one with lower and one with larger accumulated damage than 1). However, if the total damage is less than unity after the evaluated number of cycles, a linear extrapolation is conducted by using the last non-zero damage increment in the pure predeformation tests or, in the cyclic tests, by using the average of the damage increments in the last 50 loading cycles. If the damage growth is zero in all loading cycles, a large value of $N_{\mathrm{s},i}$ is returned to penalize the objective function. For the pure predeformation tests, the FE simulations have been performed for more cycles than the corresponding experiments.

It should be mentioned that, in the criteria based on the critical plane search method (see Section 4), the polar angle θ and the azimuthal angle φ are varied in steps of 5°; thus, the number of intervals in θ direction is $N_\theta = 19$, and the number of intervals in φ direction on the equatorial plane is $N_\varphi = 73$. In order to have a uniform distribution of planes over the spherical surface, for a given angle θ, the number of intervals in φ direction is obtained as $\left(N_\varphi - 1\right)\sin(\theta) + 1$.

5.1. Cross-validation

The quality of a crack initiation criterion cannot be evaluated only by its ability to fit experiments, since more independent fatigue parameters can result in a more accurate fit but might lower the criterion predictive capability (i.e. overfitting). Therefore, cross-validation [31] has been adopted to measure the performance of each criterion on new data as well as to reduce the risk of overfitting. In this method, the list of experiments (with size n) is divided into calibration data (with size $n-1$) and validation data (with size 1) in n possible ways.

In this work, we consider the pure predeformation tests under nominal axial stress ranging from −500 MPa to +250 MPa, together with subsequent cyclic tests on undeformed material (PD_0) as well as predeformed material with 3 and 6 cycles of predeformation (PD_3 and PD_6, respectively). It has been chosen to evaluate the PD(−250), PD(0), and the 3 cyclic tests for PD_3 (see Table 2) for cross-validation, to avoid extrapolating the behavior. The prediction error of each validation set $E_{p,i}$ is calculated according to Eq. (23). Then, the prediction error of a model E_{pred} is computed as the mean value of all $E_{p,i}$. Similarly, the fitting error of a model E_{fit} is computed.

6. Results

6.1. Results of the cross-validation analysis

Table 4 shows the cross-validation results for the evaluated crack initiation criteria. Considering the fitting error E_{fit}, the mixed criterion does not give a significant enhancement compared to the J-S criterion, arising from the large identified values for ϵ_c, see Table 4a. The challenge of fitting the experimental data in this study is that different types of experiments in terms of material states (i.e., isotropic and anisotropic material), loading conditions (i.e., uniaxial and multiaxial loading), and the amount of plastic strain in each loading cycle (i.e., large and small amounts of plastic strain in each cycle in the pure predeformation and cyclic tests, respectively) are considered in the calibration sets. Since we aim to model the considered experimental data for the different material states accurately enough, two modified versions of the J-S criterion were introduced in Section 4.

While the modified J-S criterion ($\widetilde{C_0}$) shows a slightly better fit compared to the J-S criterion, the modified J-S criterion ($\widetilde{FP_0}$) results in a significant improvement in the fitting, but the mean prediction error E_{pred} is relatively similar to that of the J-S model. Among the evaluated criteria, the modified J-S criterion ($\widetilde{C_0}$) gives the lowest mean prediction error (although the maximum value is a bit higher).

Considering the J-S criterion, the range of the identified values for m and J are rather close to those found in literature [32] for pearlitic steel, while the range for C_0 differs, which is probably a result of the challenge with different material states and loading conditions in the experiments. The minimum and maximum values show that the variation in the identified fatigue parameters is small.

Regarding the mixed criterion, overall, it shows a similar observation as the J-S criterion for the fatigue parameters m, C_0, and J, except for the larger variation in the identified values for C_0. In most cases, the identified values of ϵ_c are large and close to the chosen upper bound defined for this parameter, implying that the ratcheting damage is insignificant.

Fig. 9(a) shows the ratcheting strain of the pure predeformation tests for the number of torque cycles corresponding to the experiments. While ϵ_r increases during the predeformation tests, it remains almost constant during the subsequent cyclic loading, supporting the fact that ϵ_c can be identified based on only the pure predeformation tests. As can be observed in Fig. 9a, the critical strain ϵ_c shows a dependence on the loading condition. In particular, it is clear that compression is delaying fatigue crack initiation. Therefore, the identified values for ϵ_c based on the pure predeformation tests (Table 4a) are different than that in [13] based on the uniaxial low cycle fatigue tests.

Comparable results to those obtained for the J-S criterion when considering the parameters m, C_0, and J are obtained for the modified J-S criteria, $\widetilde{C_0}$ and $\widetilde{FP_0}$. The variations are large for the parameters S, FP_∞, and κ in the modified models.

As mentioned previously, considerable improvement in the fitting error is obtained for the modified J-S criterion ($\widetilde{FP_0}$) compared to the original model. However, a relatively similar prediction error, together with the rather large variation of the identified values for the introduced parameters, indicates a tendency of overfitting. One solution to address this is to reduce the model complexity by using fewer model parameters, but to consider a linear relation for the fatigue threshold in terms of ratcheting strain is unrealistic. Moreover, while the modified J-S criterion ($\widetilde{C_0}$) with less model complexity achieved a better prediction compared to the J-S criterion, it did not give a significant reduction in the fitting error. Another option to overcome overfitting is to include more experiments in the calibration set. This will be pursued in Section 6.2 by considering all the experiments in the optimization.

6.2. Parameter identification considering all experiments

The results of the cross-validation revealed that the extended criteria could fit the experimental data more accurately, without (significantly) reducing the prediction accuracy of the J-S criterion. For use in engineering purposes, it is relevant to see how well the criteria work when all experiments are included in the optimization. These results are presented in Table 5 for the J-S criterion, as well as the modified J-S criteria, $\widetilde{C_0}$ and $\widetilde{FP_0}$.

The identified parameters for each criterion are in the range of the corresponding values presented in Table 4a. Moreover, the fitting error of the modified J-S criterion ($\widetilde{FP_0}$) is still noticeably lower than that of the original model as well as the modified J-S criterion ($\widetilde{C_0}$), indicating that the more advanced model has the potential for further enhancement, if more experiments are available.

Fig. 10 shows the normalized fatigue lives for all of the experiments, comparing the J-S criterion with the two modified models in terms of fitting. As can be seen, in almost all cases, the three criteria either over- or underestimate the fatigue lives. Considering the pure predeformation tests, the modified J-S criterion ($\widetilde{C_0}$) gives a much better estimation of the fatigue life for PD(−500) than the $\widetilde{FP_0}$ criterion (and than the original model). Additionally, the modified criteria show rather similar results for the other cases (and outperform the J-S criterion in the case of the PD(−250) test). The fatigue lives during the cyclic tests are fitted significantly more accurately by the $\widetilde{FP_0}$ criterion. In summary, the modified J-S criterion ($\widetilde{FP_0}$) provides the best overall fit, as shown by the lower fitting error in Table 5. However, it should be noted that each crack initiation criterion can give a good fit for the relevant set of experiments.

The evolution of LCF damage for the pure predeformation and cyclic tests from the J-S criterion and the modified J-S criterion ($\widetilde{FP_0}$) are illustrated in Fig. 11. Note that, for the cyclic tests, the x-axis shows the lifetime on a logarithmic scale. The simulation results for the pure predeformation tests show that PD(+250) has larger fatigue damage growth compared to the tests with zero or compressive axial stresses. This is also observed from the experimental results in this figure. Regarding the cyclic tests, a large amount of fatigue damage accumulates during the predeformation part of the cyclic tests (i.e., the first 3 and 6 cycles in the PD_3 and PD_6 experiments, respectively).

Table 4
Cross-validation results from the evaluated crack initiation criteria. The values denote Mean (Minimum, Maximum).
(a) Identified fatigue parameters

Criterion	m [–]	C_0 [MPa]	J [–]	Other parameters
J-S	2.20 (2.13, 2.27)	94.1 (91.1, 99.4)	0.21 (0.18, 0.23)	–
Mixed	2.16 (1.98, 2.24)	104.8 (93.6, 139.1)	0.21 (0.18, 0.23)	ϵ_c = 14.1 (2.5, 19.9) [–]
Modified J-S ($\widetilde{C_0}$)	2.21 (2.13, 2.26)	82.9 (75.6, 99.2)	0.19 (0.17, 0.20)	S = 14.3 (0.2, 26.1) [MPa]
Modified J-S ($\widetilde{FP}_0$)	1.98 (1.81, 2.11)	102.3 (89.9, 120.2)	0.22 (0.19, 0.24)	FP_∞ = 2.09 (1.23, 2.66) [MPa] $10^3\kappa$ =63.9 (6.4, 285.5) [–]

(b) Fitting and prediction errors

Criterion	E_{fit} [%]	E_{pred} [%]
J-S	13.7 (12.1, 15.1)	22.8 (6.3, 30.2)
Mixed	13.5 (12.1, 15.2)	24.7 (6.1, 40.0)
Modified J-S ($\widetilde{C_0}$)	12.7 (10.2, 14.3)	20.9 (3.3, 35.7)
Modified J-S ($\widetilde{FP_0}$)	7.9 (6.6, 9.1)	22.6 (5.8, 37.4)

Table 5
Identified fatigue parameters when all experiments are considered in the optimization.

Criterion	m [–]	C_0 [MPa]	J [–]	S [MPa]	FP_∞ [MPa]	$10^3\kappa$ [–]	E_{fit} [%]
J-S	2.22	91.2	0.20	–	–	–	14.4
Modified J-S ($\widetilde{C_0}$)	2.23	80.1	0.19	15.9	–	–	13.5
Modified J-S ($\widetilde{FP_0}$)	2.03	98.7	0.23	–	2.03	9.5	8.8

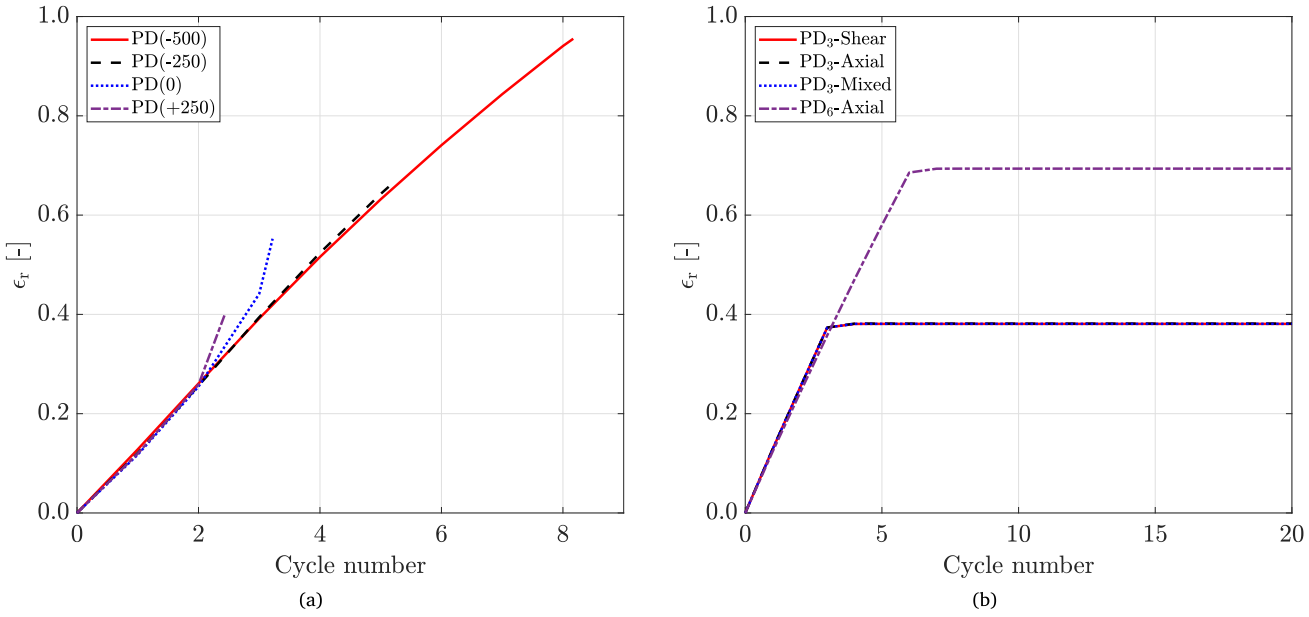

Fig. 9. Ratcheting strain evolution for (a) Pure predeformation tests, and (b) cyclic tests (except for PD_0-Shear). Note that, for the cyclic tests, only the results for the first 20 cycles are shown.

Then, the damage rate decreases, when the specimens are subjected to a small amount of uniaxial or biaxial strains in each loading cycle. In the PD_0-Shear test without any predeformation, however, the amount of damage that accumulates in each loading cycle until failure is very small. It can be mentioned that the ordering of the predicted lives is correct for the calibrated criteria compared to the experiments.

7. Concluding remarks

Experiments on R260 rail steel have been considered as a basis for the current study on crack initiation criteria. Data from three types of experiments have been used: Pure predeformation tests with combined pulsating axial and torsional loading up to failure to mimic the accumulation of shear strains in the surface layer of in-service rails, predeformation tests followed by cyclic torsion, axial, or mixed loading in the LCF range, and HCF tests to determine the fatigue damage threshold. Since the stress–strain conditions in the specimens are inhomogeneous, FE simulations have been conducted to find local stress and strain histories. The evolution of the material properties during the large deformations in the experiments significantly influences the stresses and strains in the specimens which in turn affects the predictions of fatigue crack initiation criteria. Hence, a cyclic finite strain plasticity model accounting for isotropic, kinematic, and distortional hardening of the material has been adopted to predict the stresses and strains as accurately as possible.

A cross-validation approach has been adopted to assess the performance of crack initiation criteria. As a starting point, two commonly used fatigue crack initiation criteria for rolling contact fatigue of railway steel have been used: the Jiang-Sehitoglu (J-S) criterion and the so-called mixed model that combines the J-S and the Kapoor criteria.

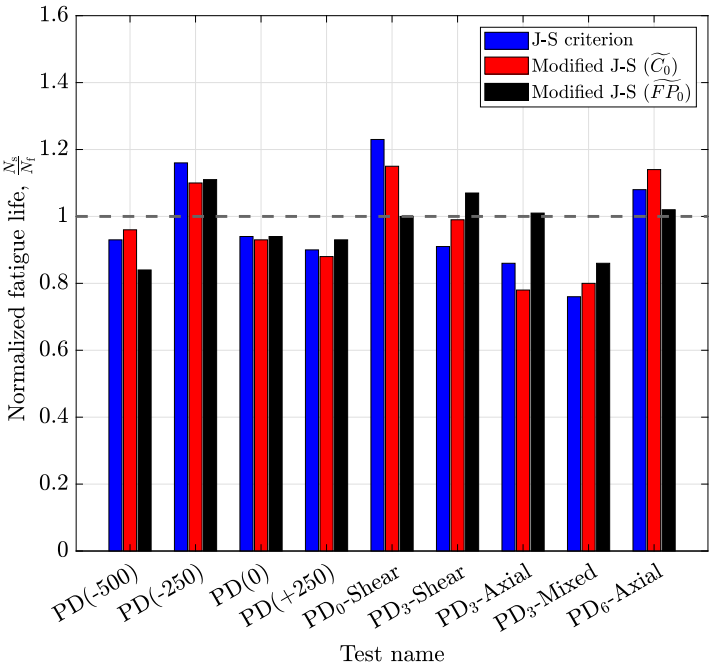

Fig. 10. Normalized fatigue lives from the J-S criterion and the modified J-S criteria, $\widetilde{C_0}$ and $\widetilde{FP_0}$. The horizontal line indicates the case where the fatigue life from the simulations equals that from the experiments.

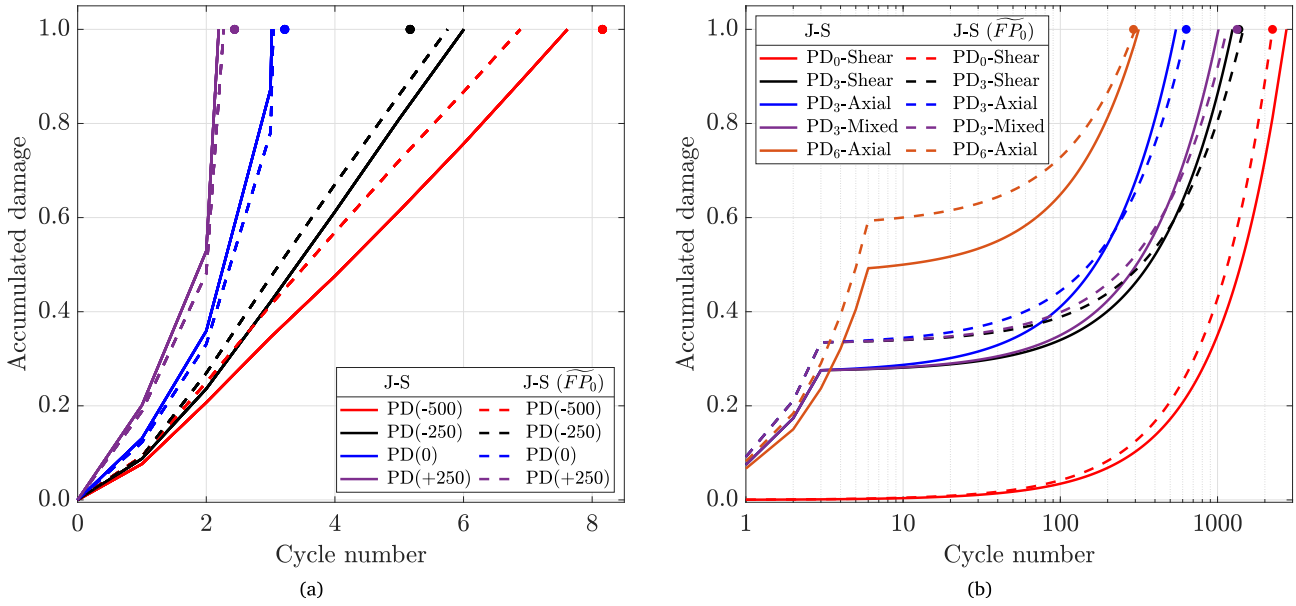

Fig. 11. Accumulated damage from the J-S criterion and the modified J-S criterion ($\widetilde{FP_0}$) for (a) Pure predeformation tests, and (b) cyclic tests. Note that, the circles show the cycle number when failure occurred in the experiments.

Compared to the J-S criterion, no improvement in the numerical predictions was found for the more advanced mixed criterion. Motivated by the protective effect of predeformation reported in the literature, we have proposed the following alternative modifications to the J-S criterion: the modified J-S criterion ($\widetilde{C_0}$) and the modified J-S criterion ($\widetilde{FP_0}$). In both models, the effect of material state influenced by predeformation has been accounted for by considering $\widetilde{C_0}$ and $\widetilde{FP_0}$ to be linearly and exponentially dependent on the ratcheting strain, respectively. The former model showed slightly improved fitting and prediction. However, the modified J-S criterion ($\widetilde{FP_0}$) resulted in a large improvement in the fitting error without (significantly) worsening the prediction. To overcome the tendency for overfitting, all of the experiments were included in the optimization. The modified J-S criterion ($\widetilde{FP_0}$) showed still promising results in terms of fitting error compared to the J-S criterion, showing the capacity of the modified model for further improvement in the case of more experiments.

CRediT authorship contribution statement

Nasrin Talebi: Conceptualization, Data curation, Formal analysis, Investigation, Methodology, Software, Validation, Visualization, Writing – original draft. **Johan Ahlström:** Supervision, Writing – review & editing. **Magnus Ekh:** Conceptualization, Funding acquisition, Methodology, Project administration, Supervision, Writing – review & editing. **Knut Andreas Meyer:** Conceptualization, Data curation, Methodology, Supervision, Writing – review & editing.

Declaration of competing interest

The authors declare that they have no known competing financial interests or personal relationships that could have appeared to influence the work reported in this paper.

Data availability

Data will be made available on request.

Acknowledgments

This work is part of the ongoing activities within the Centre of Excellence CHARMEC (www.chalmers.se/charmec). They are partially funded within the European Union's Horizon 2020 research and innovation program in the Shift2Rail project In2Track3 under grant agreement No 101012456 and in Europe's Rail project IAM4RAIL under grant agreement No 101101966. The simulations were performed on resources provided by Chalmers e-Commons (C3SE).

Appendix. Material model formulation

A summary of the model proposed by Meyer and Menzel [20] for finite strains is given here for completeness. The notations used for describing the model are given first. Second-order tensors are written in boldface, e.g. $\boldsymbol{a}$, while fourth-order tensors are written in capitalized, boldface, and upright form, e.g. $\mathbf{A}$. The non-standard open products $\underline{\otimes}$ and $\overline{\otimes}$ between two second-order tensors are respectively defined as: $\boldsymbol{a}\underline{\otimes}\boldsymbol{b} = a_{il}b_{jk}\underline{\boldsymbol{e}}_i\otimes\underline{\boldsymbol{e}}_j\otimes\underline{\boldsymbol{e}}_k\otimes\underline{\boldsymbol{e}}_l$ and $\boldsymbol{a}\overline{\otimes}\boldsymbol{b} = a_{ik}b_{jl}\underline{\boldsymbol{e}}_i\otimes\underline{\boldsymbol{e}}_j\otimes\underline{\boldsymbol{e}}_k\otimes\underline{\boldsymbol{e}}_l$. $\boldsymbol{I}$ is the second-order identity tensor, and the fourth-order deviatoric identity tensor, $\mathbf{I}^{\mathrm{dev}} = \boldsymbol{I}\overline{\otimes}\boldsymbol{I} - \boldsymbol{I}\otimes\boldsymbol{I}/3$.

The Mandel stress, $\boldsymbol{M}$, is defined as

$$\boldsymbol{M} = \frac{G\boldsymbol{C}_{\mathrm{e}}^{\mathrm{dev}}}{\mathrm{I}_{3\mathrm{C}_{\mathrm{e}}}^{1/3}} + K\left[\mathrm{I}_{3\mathrm{C}_{\mathrm{e}}} - \sqrt{\mathrm{I}_{3\mathrm{C}_{\mathrm{e}}}}\right]\boldsymbol{I} \tag{A.1}$$

where G and K are the elastic shear and bulk moduli, $\boldsymbol{C}_{\mathrm{e}} = \boldsymbol{F}_{\mathrm{e}}^{\mathrm{T}}\boldsymbol{F}_{\mathrm{e}}$ is the standard elastic Cauchy–Green deformation tensor, and $\mathrm{I}_{3\mathrm{C}_{\mathrm{e}}} = \det(\boldsymbol{C}_{\mathrm{e}})$ is the third invariant of $\boldsymbol{C}_{\mathrm{e}}$. The evolving anisotropic yield criterion, as mentioned in Section 3.2, is defined as

$$\Phi = \sqrt{\boldsymbol{M}_{\mathrm{red}}^{\mathrm{dev}} : \hat{\mathbf{C}} : \boldsymbol{M}_{\mathrm{red}}^{\mathrm{dev}}} - Y \le 0 \tag{A.2}$$

$$\hat{\mathbf{C}} = \frac{3}{2}\mathbf{C}^{\mathrm{T}} : \left[\boldsymbol{I}\underline{\otimes}\boldsymbol{I}\right] : \mathbf{C} \tag{A.3}$$

where $\hat{\mathbf{C}}$ is the anisotropy tensor, and the fourth-order tensor, $\mathbf{C}$, is described as

$$\mathbf{C} = \left[1 - b_{\mathrm{c}}\right]\mathbf{I}^{\mathrm{dev}} + b_{\mathrm{c}}\mathbf{C}_{\mathrm{c}} \tag{A.4}$$

where b_{c} is a material parameter, see Table A.6, and $\mathbf{C}_{\mathrm{c}}$ is the evolving cross hardening tensor. The reduced deviatoric Mandel stress, $\boldsymbol{M}_{\mathrm{red}}^{\mathrm{dev}}$, is defined as

$$\boldsymbol{M}_{\mathrm{red}}^{\mathrm{dev}} = \boldsymbol{M}^{\mathrm{dev}} - \sum_{i=1}^{N_{\mathrm{back}}} \boldsymbol{M}_{\mathrm{k},i}^{\mathrm{dev}} \tag{A.5}$$

where $\boldsymbol{M}_{\mathrm{k},i}^{\mathrm{dev}}$ are the back-stresses due to kinematic hardening (Bauschinger's effect), representing the yield surface's center. The back-stresses are given by their corresponding kinematic variables as

$$\boldsymbol{M}_{\mathrm{k},i}^{\mathrm{dev}} = \frac{H_{\mathrm{k},i}\boldsymbol{c}_{\mathrm{k},i}^{\mathrm{dev}}}{\det\left(\boldsymbol{c}_{\mathrm{k},i}\right)^{1/3}} \tag{A.6}$$

where $H_{\mathrm{k},i}$ are the kinematic hardening moduli, and, by introducing the kinematic deformation gradient, $\boldsymbol{F}_{\mathrm{k},i}$, the kinematic deformation tensors, $\boldsymbol{c}_{\mathrm{k},i} = \boldsymbol{F}_{\mathrm{k},i}^{-T}\boldsymbol{F}_{\mathrm{k},i}^{-1}$, are introduced.

Table A.6
Material model parameters with added back stress.

Parameters	Value	Unit	Parameters	Value	Unit
E	212	GPa	δ	0.58	–
ν	0.32	–	$H_{\mathrm{k},1}$	153	GPa
K	193	GPa	$H_{\mathrm{k},2}$	3.25	GPa
G	80.5	GPa	$H_{\mathrm{k},3}$	0.07	GPa
Y_0	352	MPa	$B_{\infty,1}$	0.39	GPa
$k_{\mathrm{iso},1}$	904	–	$B_{\infty,2}$	0.31	GPa
$k_{\mathrm{iso},2}$	16.7	–	$B_{\infty,3}$	100	GPa
$Y_{\infty,1}$	−321	MPa	c_{c}	60.6	kPa^{-1}
$Y_{\infty,2}$	320	MPa	b_{c}	−0.37	–

The isotropic hardening Y evolution is chosen to be of Voce-type. This means that the hardening Y is a nonlinear function of the accumulated equivalent plastic strain, λ, i.e.

$$Y = Y_0 + \sum_{i=1}^{2} Y_{\infty,i}\left[1 - \exp\left(-\kappa_{\mathrm{iso},i}\lambda\right)\right] \tag{A.7}$$

$$\lambda = \int_0^t \dot{\lambda}\mathrm{d}t \tag{A.8}$$

where Y_0 is the initial yield stress, $Y_{\infty,i}$ are the saturation values of isotropic hardening, $\kappa_{\mathrm{iso},i}$ are described as hardening rates, and $\dot{\lambda}$ is the plastic multiplier (rate of the accumulated equivalent plastic strain).

The material model adopts an associative evolution of the plastic flow

$$\dot{\boldsymbol{F}}_{\mathrm{p}}\boldsymbol{F}_{\mathrm{p}}^{-1} =: \boldsymbol{L}_{\mathrm{p}} = \dot{\lambda}\frac{\partial\Phi}{\partial\boldsymbol{M}} = \dot{\lambda}\boldsymbol{\nu} \tag{A.9}$$

whereas the evolution of kinematic hardening is non-associative of (a combined (nonlinear)) Armstrong–Frederick and Burlet-Cailleteuad type

$$\begin{aligned}\boldsymbol{L}_{\mathrm{k},i} &= \dot{\lambda}\left[-\boldsymbol{\nu} + \boldsymbol{\nu}_{\mathrm{k},i}^{*}\right] \quad \text{with} \\ \boldsymbol{\nu}_{\mathrm{k},i}^{*} &= \delta\sqrt{\mathrm{I}_{2\boldsymbol{\nu}}}\frac{\boldsymbol{M}_{\mathrm{k},i}^{\mathrm{T}}}{B_{\infty,i}} + [1-\delta]\left[\frac{\boldsymbol{M}_{\mathrm{k},i} : \boldsymbol{\nu}}{B_{\infty,i}\sqrt{\mathrm{I}_{2\boldsymbol{\nu}}}}\right]\boldsymbol{\nu}\end{aligned} \tag{A.10}$$

where the Burlet-Cailletaud extension ($\delta \neq 1$) improves model accuracy for non-proportional loading. The parameter $B_{\infty,i}$ controls the saturation of the ith back-stress, $\boldsymbol{M}_{\mathrm{k},i}$, and δ controls the relation between the Armstrong–Frederick and Burlet-Cailletaud type of kinematic hardening. The second invariant is introduced as $\mathrm{I}_{2\boldsymbol{\nu}} = \mathrm{tr}\,(\boldsymbol{\nu}\boldsymbol{\nu})$.

The evolution of anisotropy is governed by the cross-hardening tensor, which is formulated as

$$\dot{\mathbf{C}}_{\mathrm{c}} = -\dot{\lambda}c_{\mathrm{c}}d_{\mathrm{c}}\left[\mathbf{N}_{\perp}^{\mathrm{T}} :: \mathbf{C}_{\mathrm{c}}\right]\mathbf{N}_{\perp} \tag{A.11}$$

where $d_{\mathrm{c}} = 1$ MPa, c_{c} controls the cross-hardening rate, and $\mathbf{N}_{\perp}$ is represented as

$$\mathbf{N}_{\perp} = \mathbf{I}^{\mathrm{dev}} - \boldsymbol{N}\otimes\boldsymbol{N} \tag{A.12}$$

$$\boldsymbol{N} = \frac{\left[\boldsymbol{M}_{\mathrm{red}}^{\mathrm{dev}}\right]^{\mathrm{T}}}{\sqrt{\mathrm{I}_{2\boldsymbol{M}_{\mathrm{red}}^{\mathrm{dev}}}}} \tag{A.13}$$

The values of the material parameters are given in Table A.6. In addition to the parameters from [20], a small kinematic hardening contribution has been added with the parameters $H_{\mathrm{kin},3}$ and $B_{\infty,3}$, as discussed in Section 3.2.

References

[1] Ekberg A, Åkesson B, Kabo E. Wheel/rail rolling contact fatigue – Probe, predict, prevent. Wear 2014;314(1):2–12.
[2] Cannon DF, Edel K, Grassie SL, Sawley K. Rail defects: an overview. Fatigue Fract Eng Mater Struct 2003;26(10):865–86.
[3] Ekberg A. INNOTRaCK deliverable 4.2.6: recommendation of, and scientific basis for minimum action rules and maintenance limits. Technical report, Paris: International Union of Railways; 2009, p. 59.

[4] Larijani N, Brouzoulis J, Schilke M, Ekh M. The effect of anisotropy on crack propagation in pearlitic rail steel. Wear 2014;314(1–2):57–68.
[5] Wetscher F, Stock R, Pippan R. Changes in the mechanical properties of a pearlitic steel due to large shear deformation. Mater Sci Eng A 2007;445–446:237–43.
[6] Leitner T, Hohenwarter A, Pippan R. Anisotropy in fracture and fatigue resistance of pearlitic steels and its effect on the crack path. Int J Fatigue 2019;124:528–36.
[7] Meyer KA, Nikas D, Ahlström J. Microstructure and mechanical properties of the running band in a pearlitic rail steel: Comparison between biaxially deformed steel and field samples. Wear 2018;396–397:12–21.
[8] Sadeghi F, Jalalahmadi B, Slack TS, Raje N, Arakere NK. A review of rolling contact fatigue. J Tribol 2009;131(4):1–15.
[9] Ringsberg JW. Life prediction of rolling contact fatigue crack initiation. Int J Fatigue 2001;23(7):575–86.
[10] Kapoor A. A re-evaluation of the life to rupture of ductile metals by cyclic plastic strain. Fatigue Fract Eng Mater Struct 1994;17(2):201–19.
[11] Golos K, Ellyin F. A total strain energy density theory for cumulative fatigue damage. J Press Vessel Technol Trans ASME 1988;110(1):36–41.
[12] Brown MW, Miller KJ. A theory for fatigue failure under multiaxial stress-strain conditions. Proc Inst Mech Eng 1973;187(1):745–55.
[13] Jiang Y, Sehitoglu H. A model for rolling contact failure. Wear 1999;224(1):38–49.
[14] Ince A, Glinka G. A generalized fatigue damage parameter for multiaxial fatigue life prediction under proportional and non-proportional loadings. Int J Fatigue 2014;62:34–41.
[15] Franklin FJ, Garnham JE, Fletcher DI, Davis CL, Kapoor A. Modelling rail steel microstructure and its effect on crack initiation. Wear 2008;265:1332–41.
[16] Trummer G, Marte C, Dietmaier P, Sommitsch C, Six K. Modeling surface rolling contact fatigue crack initiation taking severe plastic shear deformation into account. Wear 2016;352–353:136–45.
[17] Ghodrati M, Ahmadian M, Mirzaeifar R. Modeling of rolling contact fatigue in rails at the microstructural level. Wear 2018;406–407:205–17.
[18] Meyer KA, Ekh M, Ahlström J. Anisotropic yield surfaces after large shear deformations in pearlitic steel. Eur J Mech A/Solids 2020;82:103977.
[19] Christodoulou PI, Kermanidis AT, Haidemenopoulos GN. Fatigue and fracture behavior of pearlitic Grade 900A steel used in railway applications. Theor Appl Fract Mech 2016;83:51–9.
[20] Meyer KA, Menzel A. A distortional hardening model for finite plasticity. Int J Solids Struct 2021;232:111055.
[21] Ekberg A, Kabo E. Fatigue of railway wheels and rails under rolling contact and thermal loading—an overview. Wear 2005;258(7):1288–300.
[22] Reis L, Li B, De Freitas M. A multiaxial fatigue approach to Rolling Contact Fatigue in railways. Int J Fatigue 2014;67:191–202.
[23] Wong SL, Bold PE, Brown MW, Allen RJ. A branch criterion for shallow angled rolling contact fatigue cracks in rails. Wear 1996;191(1–2):45–53.
[24] Dassault Systèmes. Abaqus. 2020.
[25] Meyer KA, Ahlström J. The role of accumulated plasticity on yield surface evolution in pearlitic steel. Mech Mater 2023;179:104582.
[26] Meyer KA. Material models. 2022, [Online]. Available: github.com/KnutAM/MaterialModels.
[27] Meyer KA, Ekh M, Ahlström J. Modeling of kinematic hardening at large biaxial deformations in pearlitic rail steel. Int J Solids Struct 2018;130–131:122–32.
[28] Gren D, Ahlström J. Fatigue crack propagation on uniaxial loading of biaxially predeformed pearlitic rail steel. Metals 2023;13(10):1726.
[29] Nelder JA, Mead R. A simplex method for function minimization. Comput J 1965;7(4):308–13.
[30] Gao F, Han L. Implementing the Nelder-Mead simplex algorithm with adaptive parameters. Comput Optim Appl 2012;51(1):259–77.
[31] Stone M. Cross-validatory choice and assessment of statistical predictions. J R Stat Soc 1974;36(2):111–47.
[32] Onal O, Canadinc D, Sehitoglu H, Verzal K, Jiang Y. Investigation of rolling contact crack initiation in bainitic and pearlitic rail steels. Fatigue Fract Eng Mater Struct 2012;35:985–97.